Numerical Bifurcation Analysis of Pacemaker Dynamics in a Model of Smooth Muscle Cells

H. O. Fatoyinbo, R. G. Brown, D. J. W. Simpson & B. van Brunt

Springer

Springer

Society for Mathematical Biology

ORIGINAL ARTICLE

Check for updates

Numerical Bifurcation Analysis of Pacemaker Dynamics in a Model of Smooth Muscle Cells

H. O. Fatoyinbo[1] · R. G. Brown[1] · D. J. W. Simpson[1] · B. van Brunt[1]

Abstract

Evidence from experimental studies shows that oscillations due to electro-mechanical coupling can be generated spontaneously in smooth muscle cells. Such cellular dynamics are known as *pacemaker dynamics*. In this article, we address pacemaker dynamics associated with the interaction of Ca^{2+} and K^+ fluxes in the cell membrane of a smooth muscle cell. First we reduce a pacemaker model to a two-dimensional system equivalent to the reduced Morris–Lecar model and then perform a detailed numerical bifurcation analysis of the reduced model. Existing bifurcation analyses of the Morris–Lecar model concentrate on external applied current, whereas we focus on parameters that model the response of the cell to changes in transmural pressure. We reveal a transition between Type I and Type II excitabilities with no external current required. We also compute a two-parameter bifurcation diagram and show how the transition is explained by the bifurcation structure.

Keywords Smooth muscle cells · Electro-mechanical coupling · Pacemaker dynamics · Morris–Lecar · Saddle-node on an invariant circle bifurcation · Type I and II excitability

Mathematics Subject Classification 37N25 · 74H60 · 37M20 · 37C75 · 92C30

✉ H. O. Fatoyinbo
  H.Fatoyinbo@massey.ac.nz

  R. G. Brown
  R.G.Brown@massey.ac.nz

  D. J. W. Simpson
  D.J.W.Simpson@massey.ac.nz

  B. van Brunt
  B.vanBrunt@massey.ac.nz

1   School of Fundamental Sciences, Massey University, Palmerston North, New Zealand

Springer

1 Introduction

Electro-mechanical coupling (EMC) refers to the contraction of a smooth muscle cell (SMC) due to its excitation in response to an external mechanical stimulation, such as a change in transmural pressure, that is, the pressure gradient across the vessel wall (Ran et al. 2019). In some SMCs, EMC activity can be spontaneous owing to interactions between ion fluxes through voltage-gated ion channels. Based on experimental observations (cf. Casteels et al. 1977; Harder 1984), the ion channels coordinating the EMC activity in SMCs of feline cerebral arteries are the voltage-gated Ca^{2+} channel, voltage-gated K^+ ion channel and the leak ion channel. The spontaneous depolarisation of the cell membrane leads to the opening and closing of ion channels resulting in a fluctuation of ionic currents that can induce EMC activity (Sui et al. 2003; Brading 2006; Mahapatra et al. 2018). This pacemaker EMC activity varies across species of SMCs (Savineau and Marthan 2000) and understanding the impact of these dynamics on the type of excitability may suggest therapeutic strategies for treating diseases related to SMCs.

Under normal physiological conditions, the cell membrane of SMCs do not oscillate in the absence of external sources; however, several exceptions have been observed. Mclean and Sperelakis (1977) studied the spontaneous contraction of cultured vascular SMCs in chick embryos. Lusamvuku et al. (1979) observed spontaneous electrical activity in rabbit cerebral arteries exposed to high pressure. Harder (1984) examined cellular mechanisms of the myogenic response, the pressure-induced contraction of blood vessels to regulate blood flow, in feline middle cerebral arteries by recording intracellular electrical activity of arterial muscle cells upon elevation of transmural pressure. It was observed that the blood vessels contract and spontaneous firing occurs as the arterial blood pressure is increased. Also in vitro, Osol and Halpern (1988) observed that the spontaneous cyclic oscillations and EMC activity in cerebral arteries from genetically hypertensive rat depend on transmural pressure and temperature. Llinas (1988) experimentally explored auto-rhythmic electrical properties in the mammalian central nervous system. Meister et al. (1991) and Gu (2013b) reported experimental observations of spontaneous oscillations induced by modulating either extracellular calcium or potassium concentrations in neural cells.

Studying the collective behaviour of a population of coupled SMCs is difficult due to complex interactions between the cellular components within the vascular wall. Advancements in technology now enable these interactions to be simulated at a large scale. Multiple researchers have built integrated multi-scale computational models of an arterial segment incorporating large populations of coupled arterial components (cf. Shaikh et al. 2011; Thorne et al. 2011; He et al. 2015; Bianchi et al. 2019). These models allow for simulations of populations of coupled SMCs, and the results may be compared directly with experimental and clinical findings. To this end, Shaikh et al. (2011) studied Ca^{2+} dynamics of SMCs in an arterial segment through large coupled populations of endothelial cells (ECs) and SMCs with a large-scale computational model implemented on an IBM Blue Gene/L computing architecture (available at bluefern). Their model is based on the work of Koenigsberger et al. (2005), where cases of homocellular and heterocellular couplings are considered.

Motivated by the work of Shaikh et al. (2011), we propose a model to study the dynamics of a population of coupled SMCs. EMC has been observed in the absence of ECs (Haddock et al. 2002; Lamboley et al. 2003); thus, we will not consider ECs in the model. The SMCs are coupled through gap junctions which can be one of three types: Ca^{2+}, inositol triphosphate (IP_3) or membrane potential (electrical). A wider aim of our research is to analyse the dynamics of the SMCs through membrane potential coupling by extending the work of Gonzalez-Fernandez and Ermentrout (1994) on pacemaker vasomotion in small arteries. In this present work, we will investigate the dynamics of the membrane potential in a single SMC.

The dynamics of electrical activity in cell membranes are nonlinear and often well-modelled by a nonlinear system of ordinary differential equations (ODEs) (Izhikevich 2007; Ma and Tang 2015). Many such models have been developed to describe the behaviour of excitable cells in the cell membrane. The pioneering work of Hodgkin and Huxley describes the conduction of electrical impulses along a squid giant axon (Hodgkin and Huxley 1952). Other well-known models include the FitzHugh–Nagumo model (FitzHugh 1961; Nagumo et al. 1962), the Morris–Lecar model (Morris and Lecar 1981), the Hindmarsh–Rose model (Hindmarsh and Rose 1984), and the Izhikevich model (Izhikevich 2007).

As revealed in experiments, the electrical activity of a single excitable cell has a variety of possible dynamical behaviours, such as a rest or quiescent state, simple oscillatory motion, and complex oscillatory motion. A model of a cell can transition from one state to another as parameters are varied (Gu 2013a, b). These changes can be understood by identifying critical parameter values (bifurcations) at which the dynamical behaviour changes qualitatively (Strogatz 1994; Kuznetsov 1995; Meiss 2007). For excitable cells, arguably the most important transition is from rest to an oscillatory state (or vice versa). Bifurcations associated with this and other transitions have been identified in many studies (Govaerts and Sautois 2005; Tsumoto et al. 2006; Prescott et al. 2008; Storace et al. 2008; Barnett and Cymbalyuk 2014; Liu et al. 2014; Zhao and Gu 2017; Jia 2018; Mondal et al. 2018, 2019).

Research into EMC activity has shown that abnormal contraction is often associated with tissue diseases. For example, abnormal vasomotion in arteries can damage blood vessels causing hypertension over time (Humphrey and Wilson 2003) and spontaneous contraction of the urinary bladder causes urine leak (Brading 2006). Bifurcation theory has been used in understanding the generation and control of various diseases associated with excitable cells (cf. Christini et al. 1999; Xie et al. 2011; Jia et al. 2017; Jia 2018; Verma et al. 2020)

Models for excitable cells can be classified into two types depending on the nature of action potential generation. Rinzel and Ermentrout (1999) used the type of bifurcation at the onset of firing to classify excitable cells into Type I and Type II. In Type I excitability, the cell transitions from rest to an oscillatory state through a saddle-node on an invariant circle (SNIC) bifurcation. As parameters are varied to move away from the bifurcation, the frequency of the oscillations increases from zero. In contrast, for Type II excitability the transition from rest to an oscillatory state is through a Hopf bifurcation. In this case, the oscillations emerge with nonzero frequency. Rinzel and Ermentrout (1999) also concluded that their classification is consistent with the original classification of Hodgkin (1948) for the squid giant axon, see Ermentout

(1996), Rinzel and Ermentrout (1999), Crook et al. (1998) and Vreeswijk and Hansel (2001).

The Morris–Lecar model can exhibit both Type I and Type II excitability depending on the parameter regime. Rinzel and Ermentrout (1999) studied Type I and Type II excitability in the reduced Morris–Lecar model by adjusting the applied current. Tsumoto et al. (2006) and Zhao and Gu (2017) subsequently identified codimension-two bifurcations associated with a change between the two types of excitability. See also Duan et al. (2008) for a similar two-parameter bifurcation analysis of the Chay neuronal model, respectively.

Recently, there have been several studies of pacemaker dynamics in excitable cells, both theoretical (Duan and Lu 2006; Duan et al. 2008) and computational (González-Miranda 2012). The importance of the leak channel in the pacemaker dynamics of the full Morris–Lecar model has been studied by González-Miranda (2014). Also, Meier et al. (2015) confirmed the existence of spontaneous action potentials in the two-variable Morris–Lecar model. Despite many studies of pacemaker activity in SMCs having being conducted, there does not appear to have been any discussion about the types of excitabililty that can be exhibited.

The purpose of this paper is to explain the occurrence of Type I and II excitability in pacemaker dynamics. We begin in Sect. 2.1 with the three-dimensional ODE model of Gonzalez-Fernandez and Ermentrout (1994) for pacemaker dynamics in feline cerebral arteries. In Sect. 2.2, we apply a small simplification to the model which reduces the dynamics to the two-variable Morris–Lecar model with no applied current and nondimensionalise the model in Sect. 2.3.

Then in Sect. 3 we perform a detailed bifurcation analysis of the nondimensionalised model. As the primary bifurcation parameter, we use the voltage associated with the opening of the K^+ channels because experiments have revealed that action potentials can be triggered by an increase in transmural pressure (Harder 1984, 1987). We find both types of excitability and identify codimension-two bifurcations that represent endpoints for the two types of excitability. We stress that while the bifurcations we find have been described already in the Morris–Lecar model (Tsumoto et al. 2006; Zhao and Gu 2017; Jia 2018), we believe that this is the first work to describe this structure in pacemaker dynamics of SMCs. Moreover this work is a necessary first step towards understanding spatiotemporal behaviour in networks of SMCs connected electrically by gap junctions. Finally, conclusions are presented in Sect. 4.

2 Model Formulation

2.1 Muscle Cell Model

Gonzalez-Fernandez and Ermentrout (1994) consider a muscle cell model with external current set to zero to study pacemaker dynamics. The model consists of the three ODEs

$$C\frac{dv}{dt} = -g_L(v - v_L) - g_K n(v - v_K) - g_{Ca} m_\infty(v)(v - v_{Ca}), \qquad (1)$$

$$\frac{dn}{dt} = \lambda_n(v)\big(n_\infty(v, Ca_i) - n\big), \tag{2}$$

$$\frac{dCa_i}{dt} = \big(-\alpha g_{Ca} m_\infty(v)(v - v_{Ca}) - k_{Ca} Ca_i\big)\rho(Ca_i), \tag{3}$$

where v is the membrane potential, n is the fraction of open potassium channels, and Ca_i is the cytosolic concentration of calcium. The system parameters g_L, g_K, and g_{Ca} are the maximum conductances for the leak, potassium, and calcium currents, respectively, while v_L, v_K and v_{Ca} are the corresponding Nernst reversal potentials. Also C is the cell capacitance, k_{Ca} is the rate constant for cytosolic calcium concentration, and ρ models the calcium buffering. The auxiliary functions in the model are:

$$m_\infty(v) = 0.5\left(1 + \tanh\left(\frac{v - v_1}{v_2}\right)\right), \tag{4}$$

$$n_\infty(v, Ca_i) = 0.5\left(1 + \tanh\left(\frac{v - v_3(Ca_i)}{v_4}\right)\right), \tag{5}$$

$$v_3(Ca_i) = -\frac{v_5}{2}\tanh\left(\frac{Ca_i - Ca_3}{Ca_4}\right) + v_6, \tag{6}$$

$$\lambda_n(v) = \phi_n \cosh\left(\frac{v - v_3(Ca_i)}{2v_4}\right), \tag{7}$$

$$\rho(Ca_i) = \frac{(K_d + Ca_i)^2}{(K_d + Ca_i)^2 + K_d(B_T)}, \tag{8}$$

where n_∞ [m_∞] is the fraction of open potassium [calcium] channels at steady state, ϕ_n is the rate constant for the kinetics of the potassium channel, K_d is the ratio of backward and forward binding rates for calcium and buffer reaction (Sala and Hernandez-Cruz 1990), and B_T is the total concentration of the buffers. For further details see Gonzalez-Fernandez and Ermentrout (1994). The parameter values of Gonzalez-Fernandez and Ermentrout (1994) are listed in Table 1.

2.2 Model Reduction

To analyse the model, we first check the effects of each ionic current on pacemaker activity. To do this, we block the conductances for the leak, Ca^{2+}, and K^+ currents in turn. Over a range of parameter values, we found that pacemaker activity persists if the leak current conductance g_L is blocked, but is absent if the conductances g_{Ca} and g_K for the Ca^{2+} and K^+ currents are blocked (Fig. 1 shows an example). This tells us that the Ca^{2+} and K^+ currents are required for pacemaker activity in the model.

We now reduce system (1)–(3) to two equations. Our reduction is based on the behaviour of the time-dependent quantity v_3. Equation (6) shows that the value of v_3 has the upper and lower bounds $v_6 + \frac{v_5}{2}$ and $v_6 - \frac{v_5}{2}$, respectively. Using the parameter values of Table 2 and a numerical solution to system (1)–(3), we see from Fig. 2 that the value of v_3 spends a high proportion of time close to its upper bound (after transient dynamics have decayed). This motivates a reduction by fixing v_3 to the value of its upper bound. We thus replace (6) with $v_3 = v_3^*$, where $v_3^* = v_6 + \frac{v_5}{2}$. See already Fig. 4

Table 1 Model parameter values are taken from Gonzalez-Fernandez and Ermentrout ([1994](#))

Parameter	Value	Unit
v_1	-22.5	mV
v_2	25.0	mV
v_4	14.5	mV
v_5	8.0	mV
v_6	-15.0	mV
Ca_3	400.0	nM
Ca_4	150.0	nM
ϕ_n	2.664	s^{-1}
v_L	-70.0	mV
v_K	-90.0	mV
v_{Ca}	80.0	mV
C	1.9635×10^{-14}	$C\,mV^{-1}$
g_L	7.854×10^{-14}	$C\,s^{-1}\,mV^{-1}$
g_K	3.1416×10^{-13}	$C\,s^{-1}\,mV^{-1}$
g_{Ca}	1.57×10^{-13}	$C\,s^{-1}\,mV^{-1}$
K_d	1.0×10^3	nM
B_T	1.0×10^5	nM
α	7.9976×10^{15}	$nM\,C^{-1}$
k_{Ca}	1.3567537×10^2	s^{-1}

which shows that the bifurcation structure of the resulting reduced model is similar to that of the full model. The equilibria undergo the same sequences of bifurcations in the same order, which indicates that the reduction does not significantly alter the qualitative dynamics. The assumption of constant v_3 reduces the number of equations to two because now v and n are decoupled from Ca_i. The reduced system is

$$C\frac{dv}{dt} = -g_L(v - v_L) - g_K n(v - v_K) - g_{ca}m_\infty(v)(v - v_{ca}), \qquad (9)$$

$$\frac{dn}{dt} = \lambda_n(v)\left(n_\infty(v) - n\right), \qquad (10)$$

where

$$n_\infty(v) = 0.5\left(1 + \tanh\left(\frac{v - v_3^*}{v_4}\right)\right), \qquad (11)$$

$$\lambda_n(v) = \phi_n \cosh\left(\frac{v - v_3^*}{2v_4}\right), \qquad (12)$$

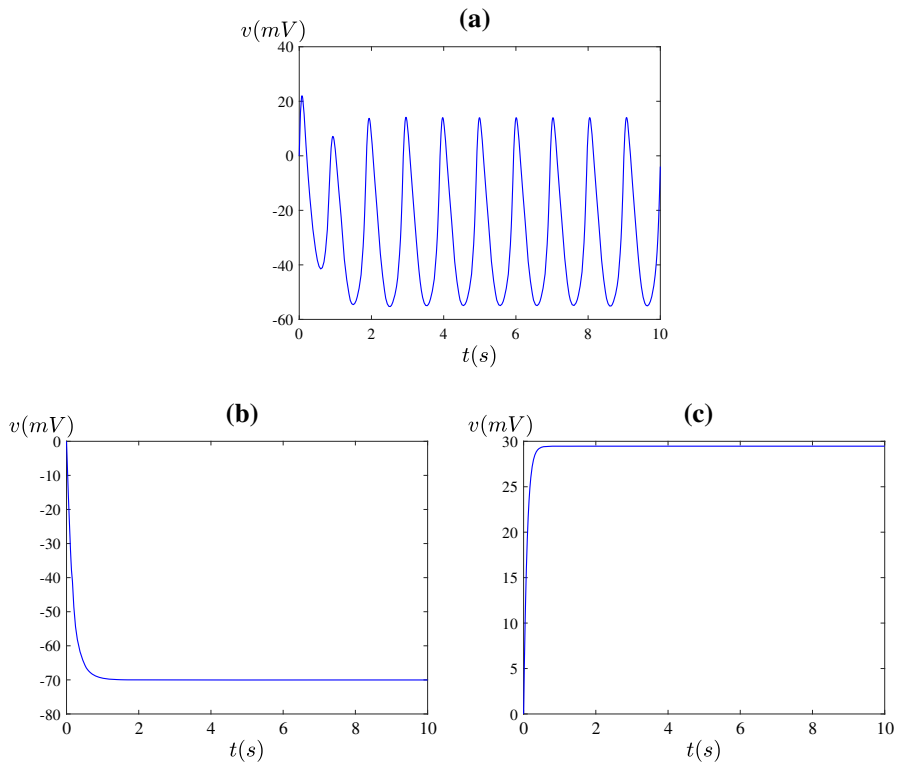and $m_\infty(v)$ is unchanged from (4). Note that this is the Morris–Lecar model without external current.

(a)

$v(mV)$

(b)

$v(mV)$

(c)

$v(mV)$

$t(s)$

Fig. 1 Time series of the membrane potential v when the three conductances are blocked: **a** the leak channel is blocked (g_L); **b** the Ca^{2+} channel is blocked (g_{Ca}); **c** the K$^+$ channel is blocked (g_K) (Color figure online)

Table 2 Parameter values for the nondimensionalised model (14)–(15)

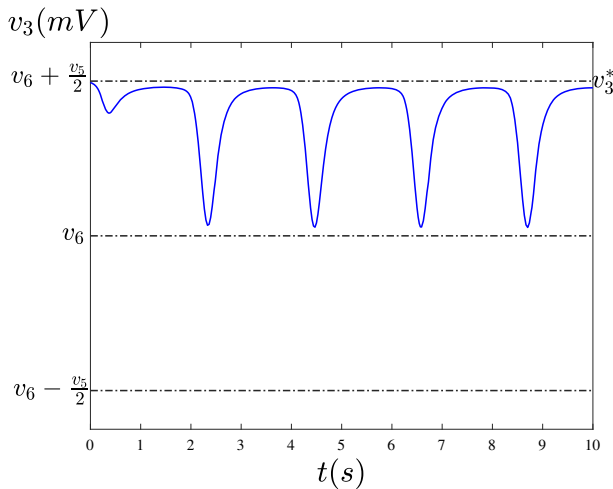| Parameter	Value
$\bar{v}_1$	-0.2813
$\bar{v}_2$	0.3125
$\bar{v}_3$	-0.1380
$\bar{v}_4$	0.1812
ψ	0.1665
$\bar{v}_L$	-0.875
$\bar{v}_K$	-1.125
$\bar{g}_L$	0.25
$\bar{g}_K$	1.0
$\bar{g}_{Ca}$	0.4997

Fig. 2 A plot of v_3 against time for solutions to (1)–(6) with the parameters of Table 1 (Color figure online)

2.3 Nondimensionalised Model

We nondimensionalise (9)–(10) by introducing dimensionless variables V and τ. Let

$$v = V Q_v, \quad t = \tau Q_t, \tag{13}$$

for some characteristic voltage Q_v and time Q_t. To choose values for Q_v and Q_t, we first observe that the range of the action potential is $v_K \leq v \leq v_{Ca}$ (see Table 1, Fig. 3a). Hence the maximum variation of the action potential is less than $v_{Ca} - v_K = 170$ mV. This value is roughly the same order of magnitude as v_{Ca}; therefore, we choose the characteristic voltage Q_v to be v_{Ca}. Simple choices for the characteristic time include $Q_t = \frac{C}{g_K} = 0.0625$ and $Q_t = \frac{1}{\phi_n} = 0.3754$. We choose $Q_t = \frac{C}{g_K}$ for the characteristic time because it is faster than $\frac{1}{\phi_n}$. Substituting $Q_v = v_{Ca}$ and $Q_t = \frac{C}{g_K}$ into (9)–(10) produces the dimensionless version of the model:

$$\frac{dV}{dT} = -\bar{g}_L(V - \bar{v}_L) - \bar{g}_K N(V - \bar{v}_K) - \bar{g}_{Ca} M_\infty(V)(V - 1), \tag{14}$$

$$\frac{dN}{dT} = \psi \lambda(V)(N_\infty(V) - N), \tag{15}$$

where

$$M_\infty(V) = 0.5 \left(1 + \tanh\left(\frac{V - \bar{v}_1}{\bar{v}_2} \right) \right), \tag{16}$$

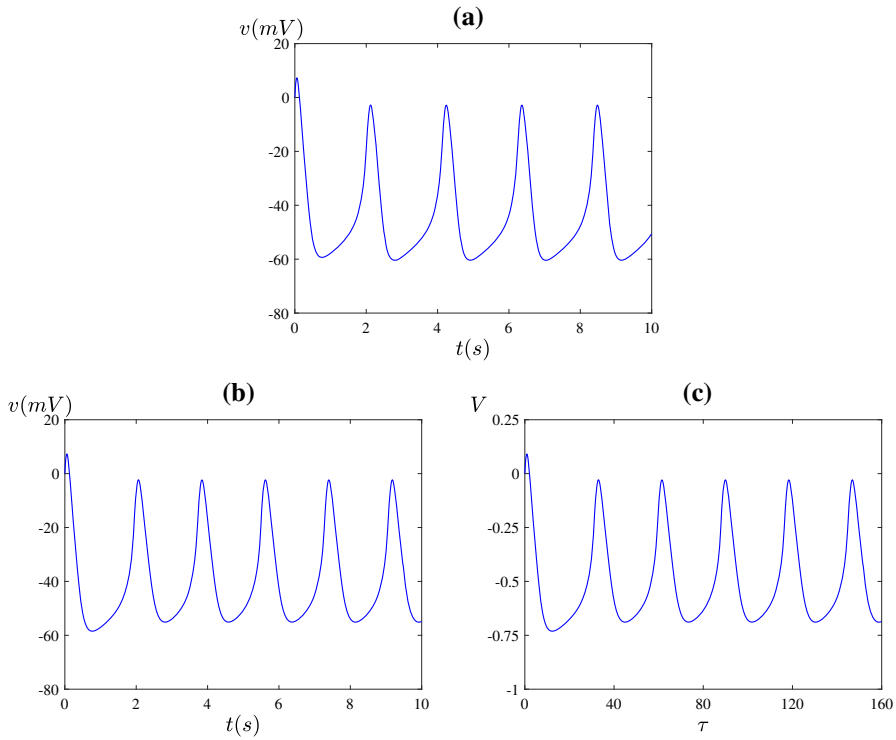$$N_\infty(V) = 0.5 \left(1 + \tanh\left(\frac{V - \bar{v}_3}{\bar{v}_4} \right) \right), \tag{17}$$

Fig. 3 A time series of the membrane potential for **a** the full model with the parameter values in Table 1 and initial condition $(v, n, \text{Ca}_i) = (0, 0, 0)$, **b** the reduced model, and **c** the nondimensionalised model with the parameter values in Table 2 and initial condition $(V, N) = (0, 0)$ (Color figure online)

$$\lambda(V) = \cosh\left(\frac{V - \bar{v}_3}{2\bar{v}_4}\right), \tag{18}$$

and

$$\bar{g}_i = \frac{g_i}{g_K}, \quad \bar{v}_i = \frac{v_i}{v_{Ca}}, \quad \psi = \frac{C\phi_n}{g_K}, \qquad i = \text{L, K, Ca, 1, 2, 3, 4.}$$

The parameter values for this model are given in Table 2.

2.4 Excitable Dynamics of the Full, Reduced, and Nondimensionalised Models

The full model (1)–(3), the reduced model (9)–(10), and the nondimensionalised model (14)–(15) were integrated numerically using the standard fourth-order Runge–Kutta method using a step size of 0.05 in the numerical software XPPAUT (Ermentrout 2002). Since our interest is primarily the membrane potential, we focus mostly on its dynamics. The time evolution of the membrane potential for the three models with the parameter values in Tables 1 and 2 reveal that they are in an oscillatory state (see
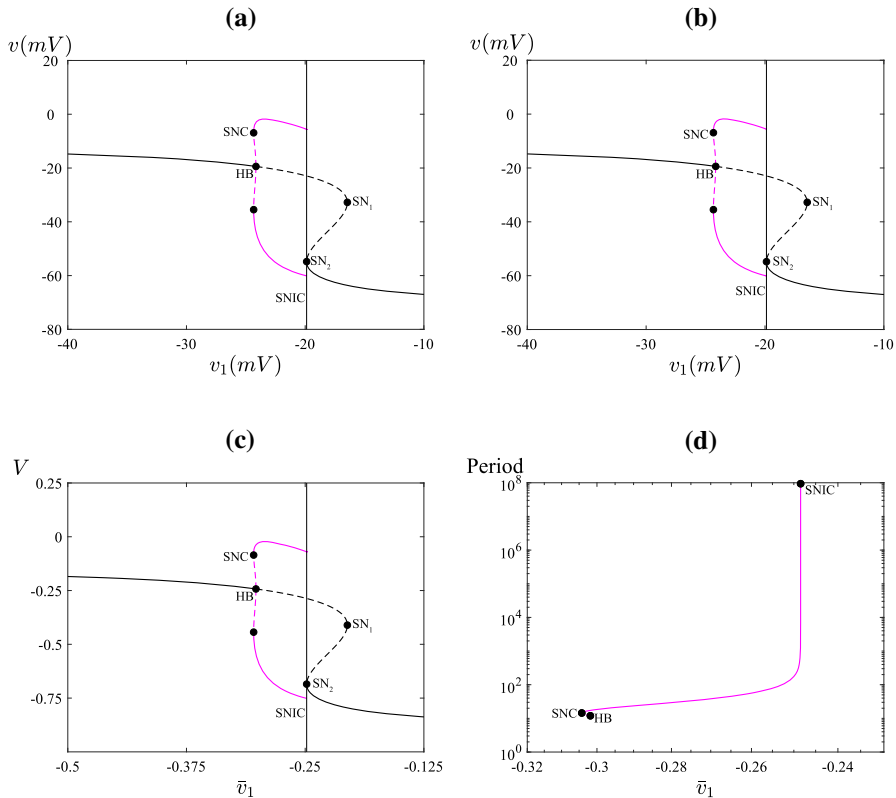
Fig. 4 Bifurcation diagrams of **a** the full model (1)–(3) with v_1 as the bifurcation parameter, **b** the reduced model (9)–(10) with v_1 as the bifurcation parameter and **c** the nondimensionalised model (14)–(15) with $\bar{v}_1$ as the bifurcation parameter. The remaining parameter values are given in Tables 1 and 2. Panel **d** shows the period of the oscillations in Fig. 4c for the nondimensionalised model. Black [magenta] curves correspond to equilibria [periodic orbits]. Solid [dashed] curves correspond to stable [unstable] solutions. HB: Hopf bifurcation; SN: saddle-node bifurcation (of an equilibrium); SNC: saddle-node bifurcation of a periodic orbit; SNIC: saddle-node on an invariant circle bifurcation (Color figure online)

Fig. 3). These self-sustained oscillations are consistent with the work of González-Miranda (2014) on pacemaker dynamics for the full Morris–Lecar model when the external current and the leak conductance are set to zero.

Next, we verify the excitability property of the model by varying the voltage associated with the fraction of open K$^+$ channels as a bifurcation parameter. Since v_1 is dependent on transmural pressure (Gonzalez-Fernandez and Ermentrout 1994), it is considered to be the main bifurcation parameter in the full model. For the reduced model, this parameter is $\bar{v}_1$. We choose a range of values of v_1 and $\bar{v}_1$ for which the systems either converge to a steady state (absence of vasomotion) or oscillate (presence of vasomotion). We use values of v_1 between -40 and -10 mV, which corresponds to values of $\bar{v}_1$ between -0.5 and -0.125. Figure 4a–c shows the bifurcation diagrams of the full, reduced and nondimensionalised models. A detailed discussion of

the bifurcation diagrams, particularly for the nondimensionalised model, is given in Sect. 3.

3 Bifurcation Analysis of Type I and Type II Excitability

Here we investigate the dynamics of the nondimensionalised model (14)–(15) via a bifurcation analysis. In Sect. 3.1, the influence of different model parameters on model behaviour is considered. Then in Sect. 3.2 we relate transitions between Type I and Type II excitability to codimension-two bifurcations.

3.1 Changes to the Dynamics as One Parameter is Varied

As shown in Fig. 3c, the nondimensionalised model exhibits stable oscillations for the parameter values of Table 2. Here we study how the dynamics changes as the parameters $\bar{v}_1$, $\bar{v}_3$, and $\bar{v}_L$ are varied from their values in Table 2. First we consider $\bar{v}_1$. A bifurcation diagram is shown in Fig. 4c. We observe the system has a unique equilibrium except between two saddle-node bifurcations, SN_1 and SN_2. To the right of SN_2 the lower equilibrium branch is the only stable solution of the system. The saddle-node bifurcation SN_2 is in fact a SNIC bifurcation (saddle-node on an invariant circle) as here there exists an orbit homoclinic to the equilibrium (Kuznetsov 1995). To the left of SN_2, this orbit persists as a stable periodic orbit. Thus here (14)–(15) model SMC activity with Type I excitability (Hodgkin and Huxley 1952; Ermentout 1996; Izhikevich 2007). As we pass through the SNIC bifurcation by decreasing the value of $\bar{v}_1$, the excitable state changes to periodic oscillations. As shown in Fig. 4d, the period of the oscillations decreases from infinity as a consequence of the homoclinic connection.

Upon further decrease in the value of $\bar{v}_1$, the stable periodic orbit loses stability in a saddle-node bifurcation (SNC). The resulting branch of unstable periodic orbits terminates in a subcritical Hopf bifurcation (HB). Between these bifurcations, the system is bistable because the upper equilibrium branch is stable to the left of the Hopf bifurcation.

Next we vary the value of the parameter $\bar{v}_3$. This is because it is of biological interest to understand the influence of transmural pressure. In the full model (1)–(3), transmural pressure is associated with the parameter v_6, so in the nondimensionalised model it is associated with $\bar{v}_3$ through $v_3^* = v_6 + \frac{v_5}{2}$. Hence we can examine the influence of transmural pressure by using $\bar{v}_3$ as a bifurcation parameter.

As shown in Fig. 5a, as we increase the value of $\bar{v}_3$ a unique equilibrium loses stability in a supercritical Hopf bifurcation HB_1 then regains stability in a subcritical Hopf bifurcation HB_2. Therefore in this case the system exhibits Type II excitability. The stable oscillations are created in HB_1 with finite period (see Fig. 5b). They subsequently lose stability at the saddle-node bifurcation SNC and terminate at HB_2.

Lastly, variation of $\bar{v}_L$ produces the bifurcation diagram Fig. 6. This has the same type of bifurcation structure as Fig. 4b (except in reverse). Thus increasing the value
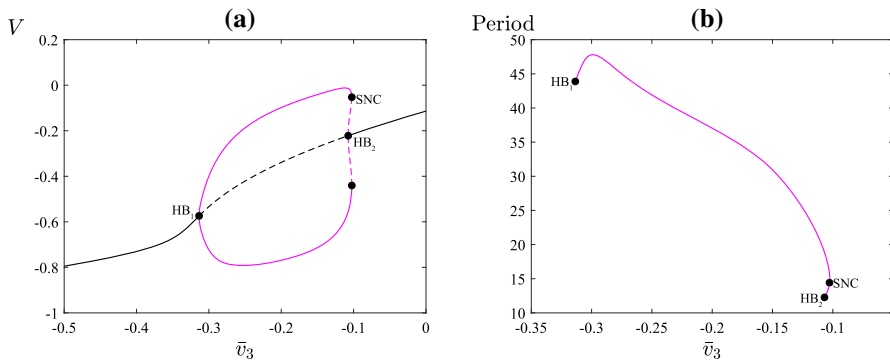
Fig. 5 **a** A bifurcation diagram of the nondimensionlised model (14)–(15) with $\bar{v}_3$ as the bifurcation parameter and other parameter values as given in Table 2. **b** A plot of the periodic oscillations as a function of parameter $\bar{v}_3$. The labels and other conventions are as in Fig. 4 (Color figure online)
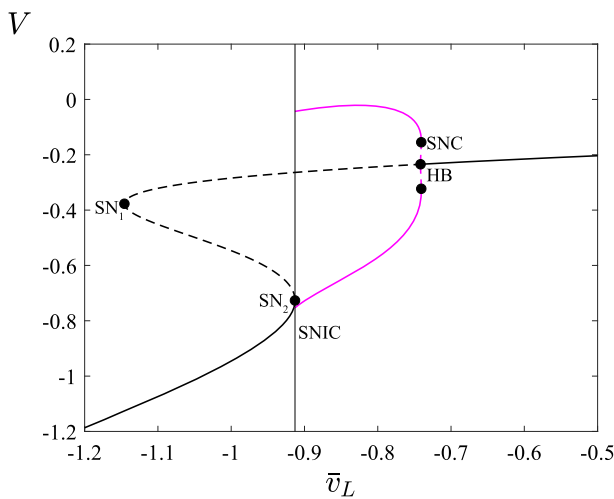

Fig. 6 A bifurcation diagram of the nondimensionalised model (14)–(15) with $\bar{v}_L$ as the bifurcation parameter and other parameter values as given in Table 2. The labels and other conventions are as in Fig. 4 (Color figure online)

of $\bar{v}_L$ results in the same qualitative changes to the dynamics as decreasing the value of $\bar{v}_1$. In particular the excitability is Type I.

3.2 Transitions Between Types of Excitability

In this section, we perform a two-parameter bifurcation analysis of the nondimension-alised model (14)–(15) by varying the parameters $\bar{v}_1$ and $\bar{v}_3$. This is summarised by the two-parameter bifurcation diagram, Fig. 7, which was produced via the numeri-cal continuation software AUTO-07p (Doedel et al. 2012). Two of the one-parameter bifurcation diagrams described above are slices of Fig. 7. Specifically Fig. 4c has the
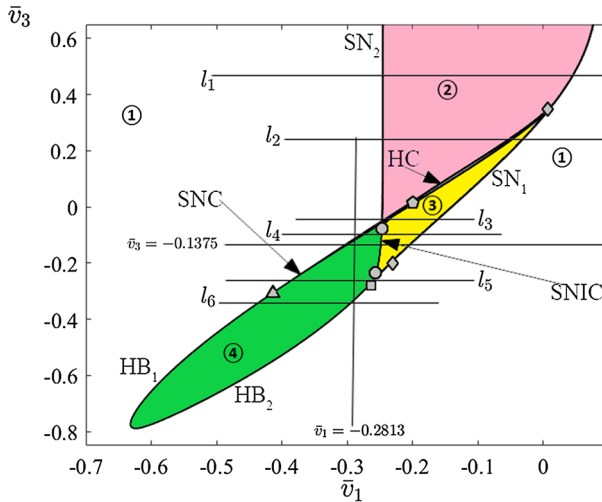
Fig. 7 A two-parameter bifurcation diagram of the nondimensionalised model (14)–(15) in the $(\bar{v}_1, \bar{v}_3)$-plane for the parameter values of Table 2. The values of $\bar{v}_3$ in l_1, l_2, l_3, l_4, l_5 and l_6 are $0.45, 0.25, -0.047, -0.088, -0.26$ and -0.32, respectively. The black curves are the loci of codimension-one bifurcations labelled as follows: HB: Hopf bifurcation, SN: saddle-node bifurcation (or SNIC), HC: homoclinic bifurcation, and SN: saddle-node bifurcation of periodic orbit. The labels for the codimension-two bifurcations are explained in Table 4. The invariant sets that exist in each region are listed in Table 3 (Color figure online)

value of $\bar{v}_3$ fixed at -0.1375 and Fig. 5a has the value of $\bar{v}_1$ fixed at -0.2813. Fig. 7 is divided into regions with eight qualitatively different types of dynamical behaviour, with enlargements in Figs. 8a, 9a, 11a and 11b. We have assigned each region a number and a colour, see Table 3.

In the remainder of this section, we describe Fig. 7 and consequences to transitions between Type I and II excitability by studying slices at six different values of $\bar{v}_3$. Fig. 7 includes five different codimension-two bifurcations summarised by Table. 4 and discussed below.

For sufficiently large values of $\bar{v}_3$, the only bifurcations are the two saddle-node bifurcations SN_1 and SN_2, see Fig. 8a which shows a magnification of Fig. 7. Thus for the slice l_1 there are no periodic solutions, Fig. 8b

As we decrease the value of $\bar{v}_3$ a Bogdanov-Takens bifurcation (Takens 1974; Bogdanov 1975), denoted BT_1, occurs on the saddle-node locus SN_1 at $\bar{v}_3 \approx 0.3792$. This is a codimension-two point from which loci of homoclinic and subcritical Hopf bifurcations emanate, denoted HC and HB_1. As known from the theory of Bogdanov-Takens bifurcations (Kuznetsov 1995) and as seen in Fig. 8a, these loci are tangent to SN_1 at the codimension-two point. Thus for a slice below BT_1, such as l_2 for which $\bar{v}_3 = 0.25$, apart from the saddle-node bifurcations already observed there are now also homoclinic and Hopf bifurcations between which there exists an unstable periodic orbit, Fig. 8c. Observe also that upon crossing BT_1 the interval of values of $\bar{v}_1$ in which the system is bistable changes from endpoints at SN_2 and SN_1 (for l_1) to endpoints at SN_2 and HB_1 (for l_2).
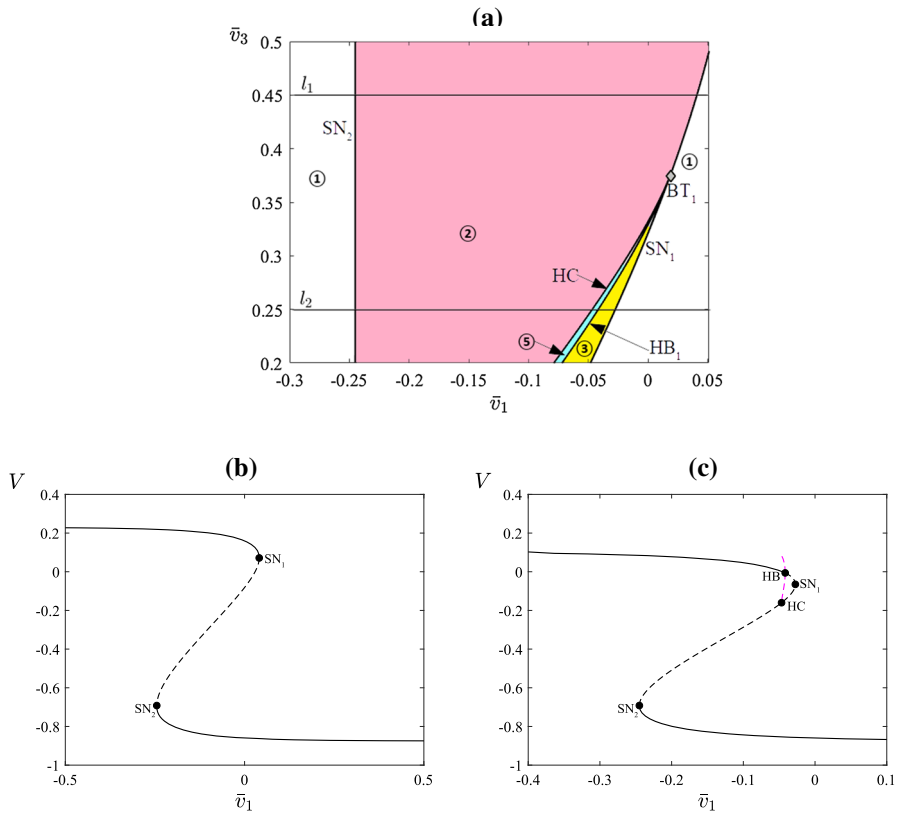
Fig. 8 **a** An enlargement of Fig. 7 showing lines l_1 and l_2. The filled diamond is a Bogdanov-Takens bifurcation. **b** A one-parameter bifurcation diagram along l_1 with $\bar{v}_3 = 0.45$. **c** A one-parameter bifurcation diagram along l_2 with $\bar{v}_3 = 0.25$. HB: Hopf bifurcation, SN: saddle-node bifurcation, SNC: saddle-node bifurcation of a periodic orbit, HC: homoclinic bifurcation (Color figure online)

As the value of $\bar{v}_3$ is decreased further, HB_1 shifts to the left and a locus of saddle-node bifurcations of the periodic orbit, SNC, emanates from the codimension-two point RHom on HC at $\bar{v}_3 \approx 0.0095$, see Fig. 9a. Thus below this point there exists a stable periodic orbit between SNC and HC, such as for the slice l_3, Fig. 9b. For this slice, as the value of $\bar{v}_1$ is decreased stable oscillations are created at HC. Here there is a small region of tristability: stable oscillations coexist with two stable equilibria, see Fig. 10.

Upon further decrease of $\bar{v}_3$, the locus HC collides tangentially with SN_2 at the codimension-two point NSH_1. This is known as a non-central saddle-node homoclinic bifurcation, see for instance (Govaerts and Sautois 2005). The collision produces the locus SNIC (saddle-node of an invariant circle). Thus immediately below NSH_1 the system exhibits Type I excitability. The system transitions from a stable equilibrium to a stable periodic orbit at the SNIC bifurcation, such as for the slice l_4, Fig. 9c (and as described earlier, Fig. 4b). Thus the point NSH_1 marks the onset of Type I excitability.
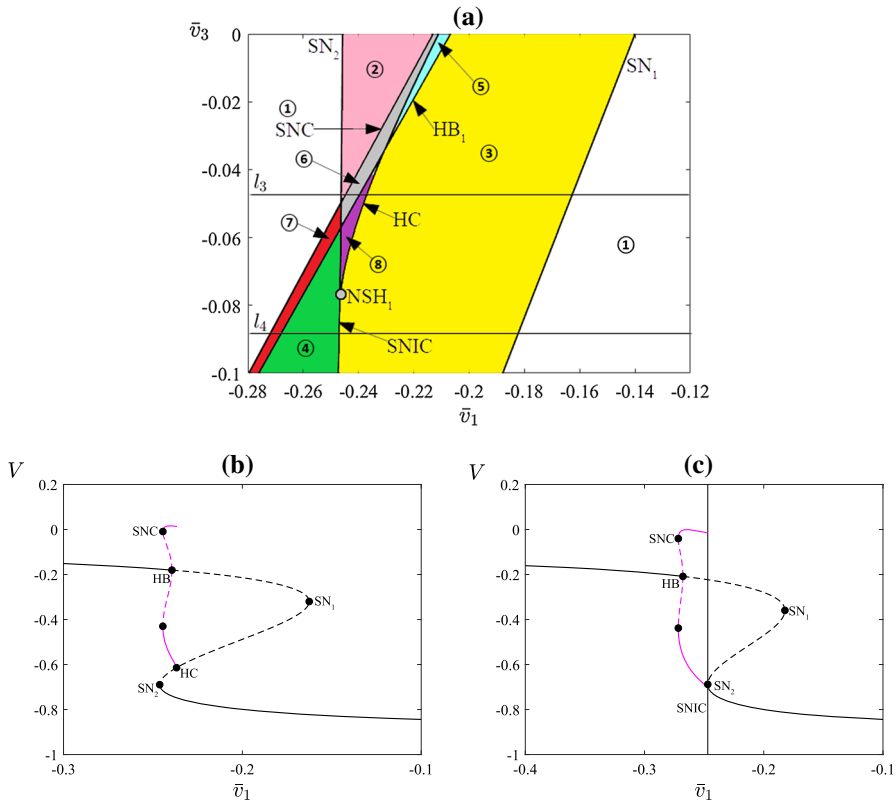
Fig. 9 a An enlargement of Fig. 7 showing lines l_3 and l_4. The filled circle is a non-central saddle-node homoclinic bifurcation. **b** A one-parameter bifurcation diagram along l_3 with $\bar{v}_3 = -0.047$. **c** A one-parameter bifurcation diagram along l_4 with $\bar{v}_3 = -0.088$. HB: Hopf bifurcation, SN: saddle-node bifurcation, SNC: saddle-node bifurcation of a periodic orbit, SNIC: saddle-node on an invariant circle bifurcation, HC: homoclinic bifurcation (Color figure online)

This has been observed previously for the reduced Morris–Lecar model with external current (Tsumoto et al. 2006).

Upon further decrease to the value of $\bar{v}_3$, a second Bogdanov-Takens bifurcation, denoted BT_2, occurs on the SN_1 locus at $\bar{v}_3 \approx -0.2429$ (see Fig. 11b). This generates loci of homoclinic and supercritical Hopf bifurcations. The homoclinic locus terminates nearby at another NSH_2 bifurcation where the SNIC locus reverts to a locus of saddle-node bifurcations. The slice l_5, Fig. 11c, is below these two codimension-two points. Here the system exhibits Type II excitability as stable oscillations are created at the Hopf bifurcation. This shows that the transition between Type I and Type II excitability for the parameter regime we have considered is governed by the Bogdanov–Takens bifurcation BT_2, and this is in agreement with the result in (Zhao and Gu 2017) where the authors studied bifurcation mechanisms induced by autapse in the Morris–Lecar model.
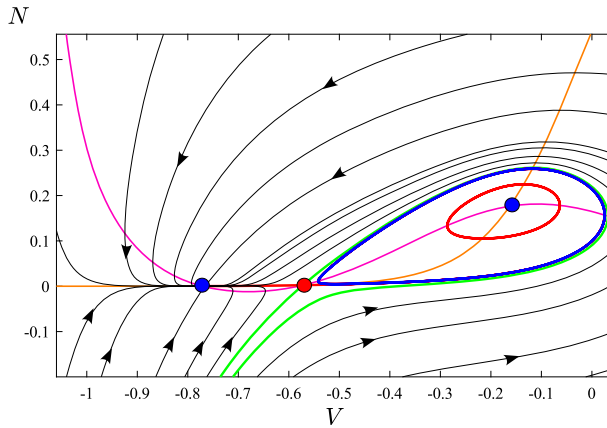
Fig. 10 A phase portrait of the nondimensionalised model (14)–(15) on line l_3 at $\bar{v}_3 = -0.047$ showing tristability. The blue and red curves are stable and unstable periodic orbits. The magenta and orange curves are the nullclines for N and V. The black curves are the solution trajectories. The blue and red circles are stable and unstable equilibria (Color figure online)
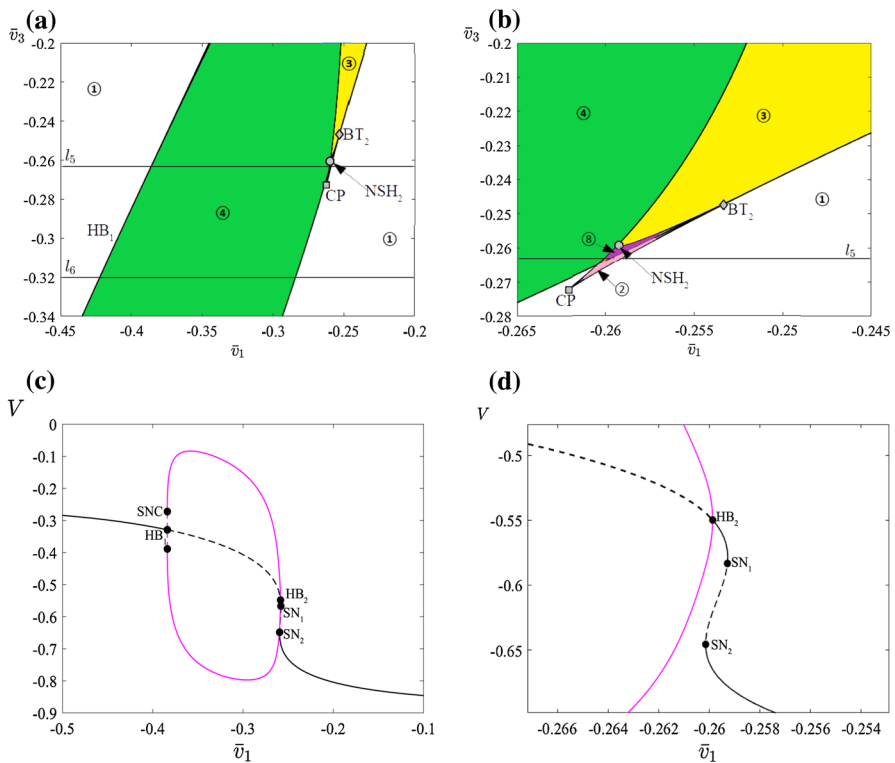

Fig. 11 **a** An enlargement of Fig. 7 showing lines l_5 and l_6, **b** an enlargement of panel (**a**). **c** A one-parameter bifurcation diagram along l_5 with $\bar{v}_3 = -0.26$. **d** An enlargement of panel (**c**). HB: Hopf bifurcation, SN: saddle-node bifurcation, SNC: saddle-node bifurcation of a periodic orbit (Color figure online)

Table 3 A summary of the eight different combinations of equilibria and periodic orbits that arise in Fig. 7 and its magnifications, Figs. 8a, 9a, 11a, and 11b

Region	Colour	Existence of equilibria and periodic orbits
①		One stable equilibrium, no periodic orbits (rest state)
②		Two stable equilibria, one unstable equilibrium, no periodic orbits
③		One stable equilibrium, two unstable equilibria, no periodic orbits
④		One unstable equilibrium, one stable periodic orbit
⑤		Two stable equilibria, one unstable equilibrium, one unstable periodic orbit
⑥		Two stable equilibria, one unstable equilibrium, one stable periodic orbit, one unstable periodic orbit (tristability)
⑦		One stable equilibrium, one stable periodic orbit, one unstable periodic orbit
⑧		One stable equilibrium, two unstable equilibria, one stable periodic orbit

Table 4 Abbreviations and notations of codimension-two bifurcations

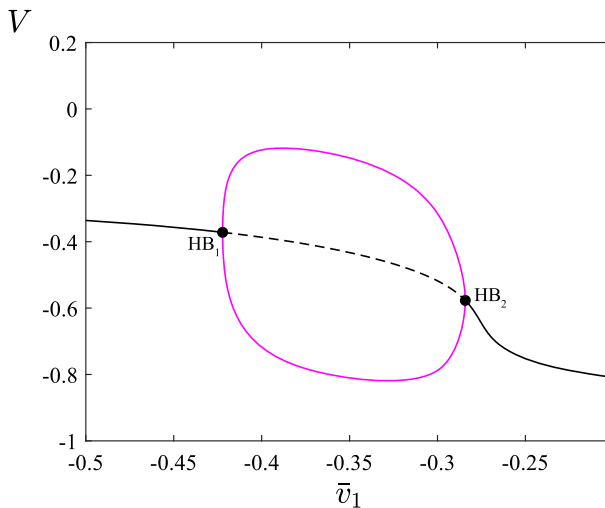| Bifurcation	Abbreviation	Label
Cusp bifurcation	CP	◻
Bogdanov-Takens bifurcation	BT_i $i = 1, 2$	◇
Generalised Hopf bifurcation	GH	△
Resonant homoclinic bifurcation	RHom	⬠
Non-central saddle-node homoclinic bifurcation	NSH_i $i = 1, 2$	◯

Fig. 12 A one-parameter bifurcation diagram along l_6 with $\bar{v}_3 = -0.32$ (shown in Figs. 7, 11a). HB: Hopf bifurcation (Color figure online)

Finally, as $\bar{v}_3$ is decreased further the Hopf locus HB_1 changes from subcritical to supercritical at a generalised Hopf bifurcation at $\bar{v}_3 \approx -0.2708$ and the saddle-node loci SN_1 and SN_2 collide and annihilate in a cusp bifurcation CP at $\bar{v}_3 \approx -0.2727$. Below these two codimension-two points, the only bifurcations that remain are two supercritical Hopf bifurcations. The slice l_6, Fig. 12, shows a typical bifurcation diagram. Here the excitability is Type II and there is no bistability.

4 Conclusion

In this paper, we have studied a pacemaker model of SMCs where the interactions between ion fluxes, in particular Ca^{2+} and K^+, results in spontaneous oscillations. We established that both Ca^{2+} and K^+ currents are required for the pacemaker activity. Upon varying the voltage associated with the opening of half the K^+ channels, v_1, the full three-dimensional model exhibits various dynamical features observed in the conventional models for excitable cells. With the aid of bifurcation diagrams, we

showed that the reduced two-dimensional model preserves the dynamical properties of the full model qualitatively.

The main motivation of this work was to understand the types of excitability exhibited by the pacemaker model. We showed that the model can be of Type I or Type II excitability depending on how parameters are varied. In particular, we determined the bifurcation structure of the $(\bar{v}_1, \bar{v}_3)$-parameter plane to show transitions between the two types of excitability. We found that, as in Tsumoto et al. (2006) which used different parameters including nonzero external current, a Bogdanov-Takens bifurcation demarcates the transition between Type I and Type II excitability.

We also revealed that the biologically important parameter $\bar{v}_1$ affects the type of excitability and nature of the oscillations more generally. The results of the model agree with experimental observations on pacemaker behaviour of smooth muscle cells (Meyer et al. 1983, 1988; Harder 1984; Segal and Duling 1989) and neural cells (Connor 1985; Ramirez et al. 2004).

It is hoped the results may find application in models and experimental studies of physiological and pathophysiological responses in muscle cells. Certainly the observation that the dynamics of SMCs are particularly sensitive to parameter values has been utilised pharmacologically in therapeutics (Droogmans and Casteels 1989; Pogátsa 1994).

Our analysis concerned a single SMC; however, SMCs are interconnected through gap junctions and action potentials can propagate between them. It remains to analyse the spatiotemporal behaviour of coupled pacemaker SMCs. Some experimental and computational studies of SMCs have shown that voltage-dependent inward Na^+ current is important in EMC activity (Berra-Romani et al. 2005; Ulyanova and Shirokov 2018), in future work we will incorporate the Na^+ current into our model to study its effect on pacemaker dynamics of SMCs.

Supplementary Information

XPPAUT was used for numerical integration, AUTO-07p for bifurcation analysis and the figures are reproduced in MATLAB. The codes are available from the corresponding author upon request.

References

Barnett W, Cymbalyuk G (2014) A codimension-2 bifurcation controlling endogenous bursting activity and pulse-triggered responses of a neuron model. PLoS ONE 9(1):e85451

Berra-Romani R, Blaustein MP, Matteson DR (2005) TTX-sensitive voltage-gated Na^+ channels are expressed in mesenteric artery smooth muscle cells. Am J Physiol Heart Circ Physiol 289:H137–H145

Bianchi D, Morin C, Badel P (2019) Computational modeling of arterial tissues: coupling multiscale homogenization strategies and finite element formulation. Comput Methods Biomech Biomed Eng 22(sup1):S22–S24

Bogdanov RI (1975) Versal deformations of a singular point of a vector field on the plane in the case of zero eigenvalues. Funct Anal Its Appl 9:144–145

Brading AF (2006) Spontaneous activity of lower urinary tract smooth muscles: correlation between ion channels and tissue function. J Physiol 570(1):13–22

Casteels R, Kitamura K, Kuriyama H, Suzuki H (1977) Excitation-contraction coupling in the smooth muscle cells of the rabbit main pulmonary artery. J Physiol 271(1):63–79

Christini DJ, Stein KM, Markowitz SMS, Mittal Slotwiner DJ, Lerman BB (1999) The role of nonlinear dynamics in cardiac arrhythmia control. Heart Dis 1(4):190–200

Connor JA (1985) Neural pacemakers and rhythmicity. Ann Rev Physiol 47:17–28

Crook SM, Ermentrout GB, Bower JM (1998) Spike frequency adaptation affects the synchronization properties of networks of cortical oscillators. Neural Comput 10(4):837–854

Doedel EJ, Oldeman BE, Wang X, Zhang C (2012) AUTO-07P: Continuation and bifurcation software for ordinary differential equations. Tech. rep, Montreal

Droogmans G, Casteels R (1989) Electromechanical and pharmacomechanical coupling in vascular smooth muscle. In: Sperelakis N (ed) Physiology and pathophysiology of the heart. Developments in cardiovascular medicine. Springer, Boston, pp 813–824

Duan L, Lu Q (2006) Codimension-two bifurcation analysis on firing activities in Chay neuron model. Chaos Solitons Fractals 30(5):1172–1179

Duan L, Lu Q, Wang Q (2008) Two-parameter bifurcation analysis of firing activities in the Chay neuronal model. Neurocomputing 72(1–3):341–351

Ermentout B (1996) Type I membranes, phase resetting curves and sychrony. Neural Comput 8(5):979–1001

Ermentrout B (2002) Simulating, analyzing, and animating dynamical systems: a guide to XPPAUT for researchers and students. SIAM Press, Philadelphia

FitzHugh R (1961) Impulses and physiological states in theoretical model of nerve membrane. Biophys J 1:445–466

Gonzalez-Fernandez JM, Ermentrout B (1994) On the origin and dynamics of the vasomotion of small arteries. Math Biosci 119:127–167

González-Miranda JM (2012) Nonlinear dynamics of the membrane potential of a bursting pacemaker cell. Chaos 22(1):013123

González-Miranda JM (2014) Pacemaker dynamics in the full Morris–Lecar model. Commun Nonlinear Sci Numer Simul 19:3229–3241

Govaerts W, Sautois B (2005) The onset and extinction of neural spiking: a numerical bifurcation approach. J Comput Neurosci 18(3):265–274

Gu H (2013a) Biological experimental observations of an unnoticed Chaos as simulated by the hindmarshrose model. PLoS ONE 8(12):e81759

Gu H (2013b) Experimental observation of transition from chaotic bursting to chaotic spiking in a neural pacemaker. Chaos 23(2):023126

Haddock RE, Hirst GD, Hill CE (2002) Voltage independence of vasomotion in isolated irideal arterioles of the rat. J Physiol 540:219–229

Harder DR (1984) Pressure-dependent membrane depolarization in cat middle cerebral artery. Circ Res 55:197–202

Harder DR (1987) Pressure-induced myogenic activation of cat cerebral arteries is dependent on intact endothelium. Circ Res 60:102–107

He F, Hua L, Gao L (2015) A computational model for biomechanical effects of arterial compliance mismatch. Appl Bion Biomech 2015:213236

Hindmarsh JL, Rose RM (1984) A model of neuronal bursting using three coupled first order differential equations. Proc R Soc Lond B 221:87–102

Hodgkin AL (1948) The local electric changes associated with repetitive action in a non-medullated axon. J Physiol 107(2):165–181

Hodgkin AL, Huxley AF (1952) A quantitative description of membrane current and its application to conduction and excitation in nerve. J Physiol 117(4):500–544

Humphrey JD, Wilson E (2003) A potential role of smooth muscle tone in early hypertension: a theoretical study. J Biomech 36(11):1595–1601

Izhikevich EM (2007) Dynamical systems in neuroscience: the geometry of excitability and bursting. MIT Press, Cambridge

Jia B (2018) Negative feedback mediated by fast Inhibitory autapse enhances neuronal oscillations near a Hopf bifurcation point. Int J Bifurc Chaos 28(2):1850030

Jia B, Gu H, Xue L (2017) A basic bifurcation structure from bursting to spiking of injured nerve fibers in a two-dimensional parameter space. Cogn Neurodyn 11:189–200

Koenigsberger M, Sauser R, Bé J, Meister J (2005) Role of the endothelium on arterial vasomotion. Biophys J 88:3845–3854

Kuznetsov YA (1995) Elements of applied bifurcation theory, 3rd edn. Springer, New York

Lamboley M, Schuster A, Bény JL, Meister JJ (2003) Recruitment of smooth muscle cells and arterial vasomotion. Am J Physiol 285:H562–H569

Liu C, Liu X, Liu S (2014) Bifurcation analysis of a Morris–Lecar neuron model. Biol Cybern 108(1):75–84

Llinas RR (1988) The intrinsic electrophysiological properties of mammalian neurons: insights into central nervous system function. Science 242(4886):1654–1664

Lusamvuku NA, Sercombe R, Aubineau P, Seylaz J (1979) Correlated electrical and mechanical responses of isolated rabbit pial arteries to some vasoactive drugs. Stroke 10(6):727–732

Ma J, Tang J (2015) A review for dynamics of collective behaviors of network of neurons. Sci China Technol Sci 58(12):2038–2045

Mahapatra C, Brain KL, Manchanda R (2018) A biophysically constrained computational model of the action potential of mouse urinary bladder smooth muscle. PLoS ONE 13(7):e0200712

Mclean MJ, Sperelakis N (1977) Electrophysiological recordings from spontaneously contracting reaggregates of cultured vascular smooth muscle cells from chick embryos. Exp Cell Res 104(2):309–318

Meier SR, Lancaster JL, Starobin JM (2015) Bursting regimes in a reaction–diffusion system with action potential-dependent equilibrium. PLoS ONE 10(3):1–25

Meiss JD (2007) Differential dynamical systems, 1st edn. SIAM, Philadelphia

Meister M, Wong RL, Baylor DA, Shatz CJ (1991) Synchronous bursts of action potentials in ganglion cells of the developing mammalian retina. Science 252(5008):939–943

Meyer JU, Lindbom L, Intaglietta M (1983) Pacemaker induced diameter oscillations at arteriolar bifurcations in skeletal muscle. Prog Appl Microcirc 12:264–269

Meyer JU, Borgstrom P, Intaglietta M (1988) Is vasomotion due to microvascular pacemaker cells? Prog Appl Mircocirc 15:41–48

Mondal A, Upadhyay RK, Mondal A, Sharma SK (2018) Dynamics of a modified excitable neuron model: diffusive instabilities and traveling wave solutions. Chaos 28(11):113104

Mondal A, Upadhyay RK, Ma J, Yadav BK, Sharma SK (2019) Bifurcation analysis and diverse firing activities of a modified excitable neuron model. Cogn Neurodyn 13(4):393–407

Morris C, Lecar H (1981) Voltage oscillations in the barnacle giant muscle fiber. Biophys J 35:193–213

Nagumo J, Arimoto S, Yoshizawa S (1962) An active pulse transmission line simulating nerve axon. Proc IRE 50(10):2061–2070

Osol GJ, Halpern W (1988) Spontaneous vasomotion in pressurized cerebral arteries from genetically hypertensive rats. Am J Physiol 254(1 Pt 2):H28–33

Pogátsa G (1994) Altered responsiveness of vascular smooth muscle to drugs in diabetes. In: Szekeres L, Papp JG (eds) Pharmacology of smooth muscle. Handbook of experimental pharmacology. Springer, Berlin, pp 693–712

Prescott SA, De Koninck Y, Sejnowski TJ (2008) Biophysical basis for three distinct dynamical mechanisms of action potential initiation. PLoS Comput Biol 4(10):1000198

Ramirez JM, Tryba AK, Peña F (2004) Pacemaker neurons and neuronal networks: an integrative view. Curr Opin Neurobiol 14(6):665–674

Ran K, Yang Z, Zhao Y, Wang X (2019) Transmural pressure drives proliferation of human arterial smooth muscle cells via mechanism associated with NADPH oxidase and Survivin. Microvasc Res 126:103905

Rinzel J, Ermentrout GB (1999) Analysis of neural excitability and oscillations. In: Koch C, Segev I 2nd (eds) Methods in neuronal modeling: from ions to network. MIT Press, London, pp 251–291

Sala F, Hernandez-Cruz A (1990) Calcium diffusion modeling in a spherical neuron. Relevance of buffering properties. Biophys J 57:313–324

Savineau J, Marthan R (2000) Cytosolic calcium oscillations in smooth muscle cells. News Physiol Sci 15(1):50–55

Segal SS, Duling BR (1989) Conduction of vasomotor responses in arterioles: a role for cell-to-cell coupling? Am J Physiol 256(3):H838–H845

Shaikh MA, Wall DJN, David T (2011) Macro-scale phenomena of arterial coupled cells: a massively parallel simulation. J R Soc Interface 9:972–987

Storace M, Linaro D, Lange E (2008) The Hindmarsh–Rose neuron model: bifurcation analysis and piecewise-linear approximations. Chaos 18(3):033128

Strogatz HS (1994) Nonlinear dynamics and chaos: with applications to physics, biology, chemistry and engineering, 1st edn. Perseus Books, Massachusetts

Sui G, Wu C, Fry C (2003) A description of Ca2+ channels in human detrusor smooth muscle. BJU Int 92(4):476–482

Takens F (1974) Singularities of vector fields. Publ Math IHES 43:47–100

Thorne B, Hayenga H, Humphrey J, Peirce S (2011) Toward a multi-scale computational model of arterial adaptation in hypertension: verification of a multi-cell agent based model. Front Physiol 2:20

Tsumoto K, Kitajima H, Yoshinaga T, Aihara K, Kawakami H (2006) Bifurcations in Morris–Lecar neuron model. Neurocomputing 69(4–6):293–316

Ulyanova AV, Shirokov RE (2018) Voltage-dependent inward currents in smooth muscle cells of skeletal muscle arterioles. PLoS ONE 13(4):e0194980

Verma P, Kienle A, Flockerzi D, Ramkrishna D (2020) Using bifurcation theory for exploring pain. Ind Eng Chem Res 59(6):2524–2535

Vreeswijk CV, Hansel D (2001) Patterns of synchrony in neural networks with spike adaptation. Neural Comput 13(5):959–992

Xie RG, Zheng DW, Xing JL, Zhang XJ, Song Y, Xie YB, Kuang F, Dong H, You SW, Xu H, Hu SJ (2011) Blockade of persistent sodium currents contributes to the riluzole-induced inhibition of spontaneous activity and oscillations in injured DRG neurons. PLoS ONE 6(4):e18681

Zhao Z, Gu H (2017) Transitions between classes of neuronal excitability and bifurcations induced by autapse. Sci Rep 7(1):6760